



# Efficient photo-electrochemical water splitting based on hematite nanorods doped with phosphorus

Xiaoning Wang<sup>a</sup>, Wenqiang Gao<sup>a</sup>, Zhenhuan Zhao<sup>b</sup>, Lili Zhao<sup>c</sup>, Jerome P. Claverie<sup>d,\*</sup>,  
Xiaofei Zhang<sup>a</sup>, Jianjun Wang<sup>a</sup>, Hong Liu<sup>a,c,\*</sup>, Yuanhua Sang<sup>a,\*</sup>

<sup>a</sup> State Key Laboratory of Crystal Materials, Shandong University, Jinan, 250100, PR China

<sup>b</sup> School of Advanced Materials and Nanotechnology, Xidian University, Xi'an, 710126, PR China

<sup>c</sup> Institute for Advanced Interdisciplinary Research, University of Jinan, Jinan, 250022, PR China

<sup>d</sup> Quebec Center for Functional Materials, Department of Chemistry, Université de Sherbrooke, Sherbrooke, J1K2R1, Canada

## ARTICLE INFO

### Keywords:

Hematite

Phosphorous

Photo-electrochemical

Water splitting

## ABSTRACT

The realization of an efficient photocatalytic water splitting in the absence of sacrificial agent is an important step to achieve the sustainable production of hydrogen using solar energy. Heterostructure-based photocatalysts are used to mitigate charge recombination, thus leading to the improved photoactivity. In a traditional electrochemical system, it works similarly as the heterostructure of z-scheme type which transports the photo-induced electrons to the cathode. Herein, by using a photo-electrochemical process, the production of oxygen and hydrogen was achieved with improved photocatalytic faradaic efficiency. The oxygen evolution process (OER) was improved upon modifying the hematite with phosphorous. The phosphorous doping led to a shift of the band structure toward more positive potentials, resulting in higher OER rates. The optimized electrode achieved a plateau photocurrent of 2.5 mA/cm<sup>2</sup> at 100 mW/cm<sup>2</sup> illumination.

## 1. Introduction

Access to renewable, environmentally-friendly and transportable sources of energy is a leading concern for our society. If efficiently harvested and stored, solar energy could readily fulfill our energy needs. Via photocatalytic water splitting, solar energy is converted into chemical energy. This reaction has generated significant interest [1,2], leading to the discovery of a plethora of systems with high hydrogen evolution rate. Among those, one could refer to a non-exhaustive fashion sub-10 nm TiO<sub>2</sub> nanoparticles with Pt as co-catalyst [3], defect engineered TiO<sub>2</sub> [4–6], heterostructures such as TiO<sub>2</sub>/SrTiO<sub>3</sub> [7], g-C<sub>3</sub>N<sub>4</sub>/NiS [8], carbon dots/TiO<sub>2</sub> mesocrystal [9], or MoS<sub>2</sub>/Graphene/CdS [10]. However, in most cases, a sacrificial agent, such as methanol [11], Na<sub>2</sub>S-Na<sub>2</sub>SO<sub>3</sub> [12], lactic acid [13] or triethanolamine [14] must be used. Only a few catalysts, such as GaN:ZnO and MgTa<sub>2</sub>O<sub>6-x</sub>N<sub>y</sub>/TaON [15,16] can achieve the true water splitting into H<sub>2</sub> and O<sub>2</sub>. Since the use of sacrificial agents is not a sustainable approach for energy production, the enhancement of true photocatalytic water splitting is still a challenge.

In general, a photocatalytic process consists of three basic steps: generation of an exciton upon light absorption, diffusion of the

separated charges to the reactive surfaces and oxidation and reduction reactions at the surface. To achieve water splitting, not only charge generation and separation steps must be efficient, but the valence and conduction bands must have sufficiently positive and negative potentials to oxidize and reduce water, respectively. Finally, the surface must possess the proper active sites with capability to reduce and oxidize water in H<sub>2</sub> and O<sub>2</sub>, respectively. As no single catalyst is endowed with all these properties, heterostructures whereby oxidation by holes and reduction by electrons occur in separated structures have been scrutinized in the past due to its benefitting for charge separation [17–19]. Besides this establishment of potential difference spontaneously from the semiconductors, other heterostructures with piezoelectric materials, which could convert mechanical press into electric potential, meet with the researchers' requirement in the control of charge carrier transport based on electric field [20,21].

In a conventional water electrolysis process, the anode and cathode act as holes and electrons suppliers. Thus, photocatalytic and electrochemical water splitting processes share many common steps, but the energy sources are respectively solar or electrical energy [19,22,23]. The n-type semiconductor hematite (α-Fe<sub>2</sub>O<sub>3</sub>) is a highly efficient electro-catalyst for oxygen evolution (OER) due to its deep valence

\* Corresponding authors at: State Key Laboratory of Crystal Materials, Shandong University, Jinan, 250100, PR China.

\*\* Corresponding author.

E-mail addresses: [jerome.claverie@usherbrooke.ca](mailto:jerome.claverie@usherbrooke.ca) (J.P. Claverie), [hongliu@sdu.edu.cn](mailto:hongliu@sdu.edu.cn) (H. Liu), [sangyh@sdu.edu.cn](mailto:sangyh@sdu.edu.cn) (Y. Sang).

band position. Because of its suitable band gap energy (2.0–2.2 eV), it is expected to behave as a visible-light photocatalyst. However, its photocatalytic activity is limited by the low charge mobility and high electron-hole recombination rate [24]. One-dimensional CdS/ $\alpha$ -Fe<sub>2</sub>O<sub>3</sub> [25],  $\alpha$ -Fe<sub>2</sub>O<sub>3</sub>/ZnO core-shell heterostructures [26], and branch-like  $\alpha$ -Fe<sub>2</sub>O<sub>3</sub>/TiO<sub>2</sub> structures [27] have been constructed to improve charge separation based on band structure alignment. Moreover, hematite has been used as catalyst for the OER process in photo-electrochemical (PEC) water splitting [28–30]. Doping of hematite with various elements such as Si [28,31], Sn [32], Cd [33], Ti [34], and Pt [35] has been proposed to modify its flat-band potential, to improve its charge mobility, and to reduce its electron-hole recombination. We infer that as dopant, phosphorus should be a good candidate because the doping would enhance the n-type semiconductor property of hematite and improves its electric conductivity [36,37].

In this work, hematite nanorod films deposited on titanium foils were modified with phosphorous. Doping with phosphorous improves the photo-electrochemical process (PEC), a phenomenon which is due to the combined action of photocatalytic charge generation and external charge separation. Thus, by carefully designing catalyst structure and PEC conditions, it is possible to achieve high H<sub>2</sub> production rates, which is of potential interest for renewable fuel generation.

## 2. Experimental procedures

### 2.1. Materials

All chemicals were purchased from Thermal Fisher Scientific and used without further purification. The preparation of  $\alpha$ -Fe<sub>2</sub>O<sub>3</sub> arrays on Ti foils was adapted from literature [38]. Typically, 0.601 g of FeCl<sub>3</sub>·6H<sub>2</sub>O was dissolved in 15 mL of de-ionized water ( $c = 0.15$  mol/L), followed by the addition of 1.275 g of NaNO<sub>3</sub> ( $c = 1$  mol/L) under continuous stirring. The pH was adjusted to around 2 with a diluted HCl solution to inhibit the hydrolysis of Fe<sup>3+</sup> and the solution was transferred to a 20 mL Teflon-lined autoclave. The Ti foils with 4.5 cm × 2 cm dimensions were washed by acetone and DI water thoroughly using an ultrasonic bath. The Ti foil was also added to the Teflon-lined autoclave to carry out the hydrothermal treatment at 100 °C for 8 h (Fig. S1 in the Supporting information). After treatment, the Ti foil was covered with light red materials. It was thoroughly washed with DI water and dried at 60 °C. It was then calcined in air at 500 °C for 4 h realizing the  $\alpha$ -Fe<sub>2</sub>O<sub>3</sub> supported on Ti foil. To react with phosphorus, the sample was annealed at 400 °C for 30 min under Ar flow (100 mL/min) in a tube furnace whereby a crucible boat containing NaH<sub>2</sub>PO<sub>2</sub> powder was placed upstream. The exhaust gas was treated with a 3 M CuSO<sub>4</sub> solution. Samples P1 to P8 were obtained with 5 mg, 10 mg, 15 mg, 20 mg, 25 mg, 35 mg, 50 mg, and 100 mg of NaH<sub>2</sub>PO<sub>2</sub>, respectively.

### 2.2. Characterization

The X-ray powder diffraction patterns of the samples were recorded by a Bruker D8 Advance powder X-ray diffractometer (XRD, Germany) with Cu K $\alpha$  radiation ( $\lambda = 0.15406$  nm). Raman spectra of samples were measured using a Renishaw 1000 microspectrometer with an excitation wavelength of 514.5 nm. The morphology of the samples was recorded on a HITACHI S-4800 field emission scanning electron microscope (FE-SEM, Japan). The transmission electron microscopic (TEM) images were acquired with a JEOL JEM 2100 microscope operating at 200 kV. X-ray photoelectron spectroscopy (XPS) spectra were measured using an ESCALAB 250 instrument, and the valence band maximum (VBM) measurement was also performed. UV-vis diffuse reflectance spectra (DRS) of the samples were recorded on a UV-VIS spectrophotometer (UV-2550, Shimadzu) with an integrating sphere attachment within the range of 200–800 nm, using BaSO<sub>4</sub> as reflectance standard.

### 2.3. Photo-electrochemical analyses and water splitting

The photo-electrochemical (PEC) assessment of the synthesized samples was performed using an electrochemical workstation (CHI600E, China) with a three-electrode configuration. Because there are  $\alpha$ -Fe<sub>2</sub>O<sub>3</sub> samples on both sides of the Ti foil, one side of the samples were covered with polymethyl methacrylate (PMMA), the other sides were used as the working electrodes. The Pt sheet was used as the counter electrode, the Ag/AgCl in saturated KCl was used as the reference electrode, and the KOH solution (0.1 M) was used as the electrolyte in all experiments. For OER, the current density of the working electrode was recorded with a bias voltage of  $-0.2$  V to  $0.9$  V under darkness and illumination with a 150 W xenon lamp. The photocurrent response ( $i$ - $t$ ) curves were also recorded with light on and off. The stability of the catalyst was estimated at a bias voltage of  $0.6$  V for 5 h. The Mott-Schottky plots were extracted from electrochemical impedance measurements recorded in the voltage ranging of  $-1$  V to  $0.1$  V with the oscillatory perturbation of  $10$  mV [39,40]. The water splitting processes were performed in a sealed electrochemical cell at the bias of  $0.6$  V ( $1.55$  V vs RHE). The electrolyte of  $0.1$  M KOH was degassed under vacuum in order to remove O<sub>2</sub>. The as-obtained O<sub>2</sub> and H<sub>2</sub> after 1 h and 2 h were measured by a gas chromatograph (Shiweipuxin, GC4806) with a TCD detector for all the samples to evaluate the PEC water splitting property.

## 3. Results and discussion

The morphology of the as-obtained precursors, of the ones calcined at 500 °C, and of the ones post-treated with 25 mg NaH<sub>2</sub>PO<sub>2</sub> (P5 sample) are shown in Fig. 1. The precursor has a rod-like morphology (Fig. 1a), and the morphology changes little after the calcination at 500 °C besides the smaller size of the nanorods (Fig. 1b). The sample conserves its morphology during treatment with 25 mg NaH<sub>2</sub>PO<sub>2</sub> at 400 °C (P5 sample, Fig. 1c), indicating that the morphology of the  $\alpha$ -Fe<sub>2</sub>O<sub>3</sub> is determined by the hydrothermal reaction. The TEM image (Fig. 1d) indicates that the surface of the P5 nanorods is mostly smooth, with a few isolated particles on its surface. The lattice fringe image (Fig. 1e) clearly shows the  $\alpha$ -Fe<sub>2</sub>O<sub>3</sub> crystal planes along the [101] direction. Thus, the nanorod consists of a  $\alpha$ -Fe<sub>2</sub>O<sub>3</sub> single crystal decorated in surface by a few particles. The elemental mapping of P5 (Fig. 1f) shows that Fe, O, and P atoms are homogeneously distributed within the structure. The XRD results and Raman spectra indicate that there is little structure change of the  $\alpha$ -Fe<sub>2</sub>O<sub>3</sub> during the phosphorus treatment with a low amount of NaH<sub>2</sub>PO<sub>2</sub> (25 mg). Larger NaH<sub>2</sub>PO<sub>2</sub> amounts induced a structural change (Details in Figs. S2 and S3 in the Supporting information).

The LSV curves of samples P1 to P8 and of  $\alpha$ -Fe<sub>2</sub>O<sub>3</sub> were recorded with and without light irradiation (Fig. 2a and b). As shown in Fig. 2a, the current densities of the anodes increase with increasing amounts of NaH<sub>2</sub>PO<sub>2</sub> up to P5 sample (25 mg), and then decrease for samples containing greater amounts of phosphorous (P6 and beyond). At low P content, the improvement can be attributed to the greater charge mobility imparted by the phosphorous treatment [36,37], while at higher P content the decrease could be related to the structural change occurring in the  $\alpha$ -Fe<sub>2</sub>O<sub>3</sub> as shown in the Raman spectra (Fig. S3 in the Supporting information). As shown in Fig. 2b and in the inset, the current densities under illumination are significantly larger compared to the current densities in darkness. The onset of the OER current is around  $1.65$  V vs RHE in darkness, but it shifts to around  $1.00$  V vs RHE under light irradiation. Moreover, the LSV current densities under light irradiation can be as considerable as  $2$ – $3$  mA/cm<sup>2</sup> for the samples P3, P4 and P5 at  $1.60$  V vs RHE. The LSV current densities increase and the onset points of OER shift to lower potentials from  $\alpha$ -Fe<sub>2</sub>O<sub>3</sub> to P3, however, from P4 to P8, the onset points of OER shift to higher potentials (Fig. S4 in the Supporting information). The  $i$ - $t$  curves at various potentials with light on and off confirm the light induced currents

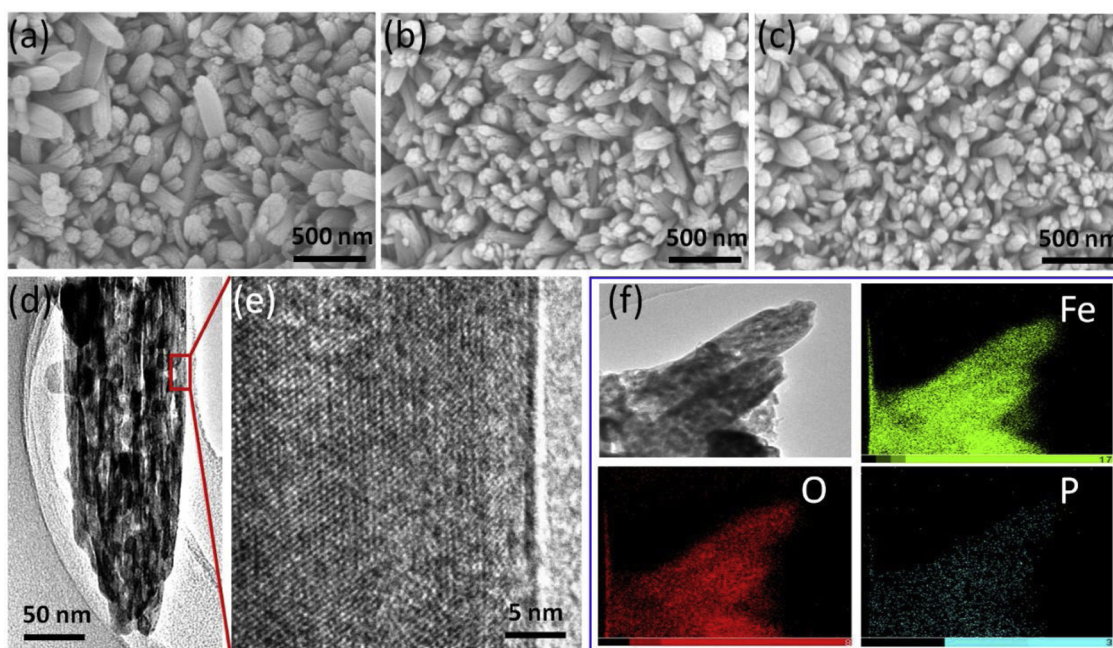


Fig. 1. SEM images of (a) the precursor obtained after 8 h hydrothermal reaction, (b) post-treated in air at 500 °C for 4 h, (c) post-treated with 25 mg  $\text{NaH}_2\text{PO}_2$  at 400 °C for 0.5 h (P5 sample), (d) TEM image of P5 sample, (e) HRTEM image of P5 sample, (f) Elemental mapping of P5 sample.

(Fig. S5 in the Supporting information). The LSV current density of P5 sample at a potential of 1.8 V vs RHE is 9.15  $\text{mA}/\text{cm}^2$ , which is much higher than the others. But it should be noticed that the current density is around 6  $\text{mA}/\text{cm}^2$  under darkness, indicating that the photo-response of P5 is similar to other samples but exhibiting a higher electrochemical property. For a better comparison of the photo-response, the absolute light induced current, which corresponds to the photocurrent minus the dark contribution, is shown in Fig. 2c. After the subtraction of the dark

current densities, the light induced currents of the various P-containing samples reach the plateau values with the increased bias voltage. For example, the absolute photo-current density of  $\alpha\text{-Fe}_2\text{O}_3$  under 120  $\text{mW}/\text{cm}^2$  solar light irradiation and at a bias of 1.8 V (vs RHE) is 0.99  $\text{mA}/\text{cm}^2$ . With phosphorous treatment, the plateau values reach 1.61, 2.71, 2.91, 2.24, and 3.17  $\text{mA}/\text{cm}^2$  for samples P1, P2, P3, P4, and P5, respectively. These different plateau values imply that the band structure of  $\alpha\text{-Fe}_2\text{O}_3$  is changed upon phosphorus treatment. As an n-type

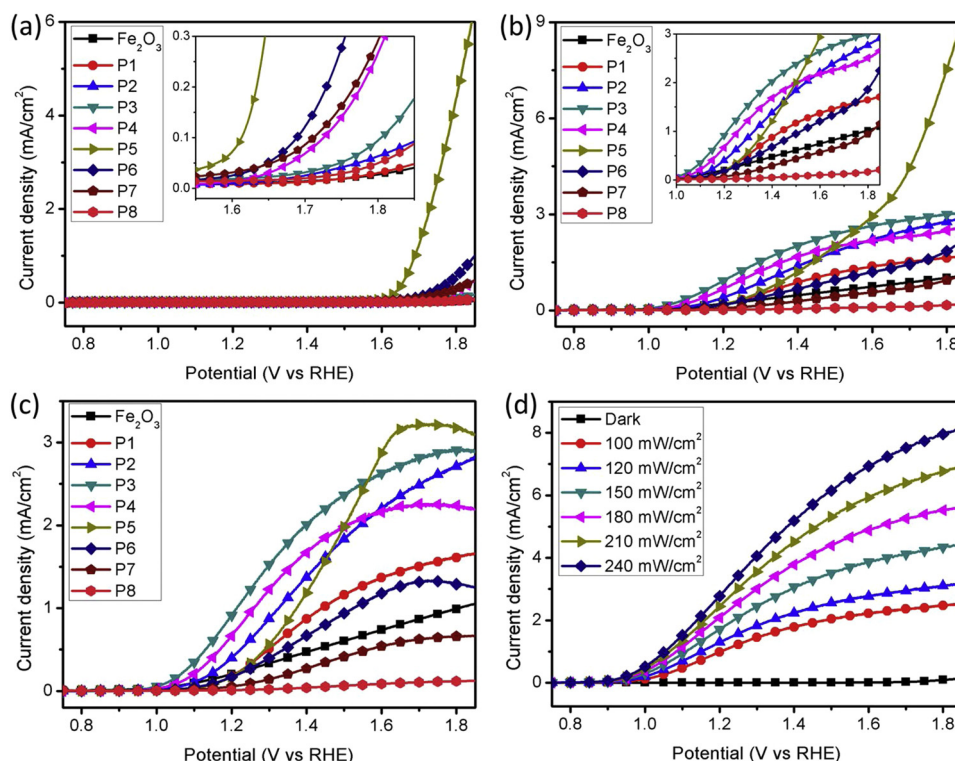


Fig. 2. LSV curves of the  $\alpha\text{-Fe}_2\text{O}_3$ , and P1 to P8 samples, (a) without and (b) with light irradiation (120  $\text{mW}/\text{cm}^2$ ). The insets are the zoom-in curves. (c) The absolute light induced currents, (d) LSV curves of P3 sample irradiated with various light intensities.



semiconductor of  $\alpha\text{-Fe}_2\text{O}_3$ , when treated with phosphorous, more electrons can be introduced in the semiconductor, resulting in an increase in charge density. The fact that a plateau is reached around 1.65 V bias seemingly indicates that the maximum number of photo-generated charges are extracted from the semiconductor at this voltage. For larger P amounts, the current densities decrease to 1.29, 0.66, and 0.12  $\text{mA}/\text{cm}^2$  for samples P6, P7 and P8, respectively. Such change can be explained by the structural change observed at this high doping level (Figs. S2 and S3).

The total OER property includes two contributions, the electrochemical one, which is mainly observed at 1.6–1.8 V vs RHE, and the photo-induced one, which is observed at bias as low as 1.0 V vs RHE. Phosphorus doping in  $\alpha\text{-Fe}_2\text{O}_3$  increases the photo-response at low concentration, but decreases it at higher concentrations. Meanwhile, phosphorus doping in  $\alpha\text{-Fe}_2\text{O}_3$  improves its electrochemical OER property, even at high concentration. Therefore, an optimized photo-electrochemical OER property is the balance between photo-response and electrochemical properties at various bias voltages. To confirm the light response of the samples, the LSV curves of samples P3, P4, and P5 irradiated with various light intensities are shown in Figs. 2d and S6 (Supporting information). When the light intensity increases from 100  $\text{mW}/\text{cm}^2$  to 240  $\text{mW}/\text{cm}^2$ , the current density of sample P3 increases from 2.5  $\text{mA}/\text{cm}^2$  to 8.2  $\text{mA}/\text{cm}^2$ . Similar results are obtained for samples P4 and P5 (Fig. S6 in the Supporting information). The LSV current density increases linearly with light intensity for all samples (Fig. S7 in the Supporting information), indicating that the photo-induced current density is proportional to the incident light density. This result indicates that photocatalytic and the electrochemical processes are independent, and that light irradiation does not influence the electrochemical OER property significantly.

Fig. 3a exhibits the reaction cell of the photo-electrochemical water splitting process, and the insets are the photographs of the sample and the Pt electrodes. The traditional 3-electrodes system was used. To realize the photo-induced water splitting instead of electrochemical water splitting, the applied bias was set at 1.55 V vs RHE (0.6 V vs Ag/AgCl@0.1 M KOH) because the electrochemical OER property can be neglected at such bias. Meanwhile, the photo-induced currents are close to plateau values, resulting in optimal photocatalytic water splitting

property. Under light irradiation, bubbles are formed on the surface of the Pt counter electrode. Fig. 3b shows the LSV curves on the OER electrode under solar light irradiation and HER electrodes without light. The inset shows the current variation based on the voltage applied between the electrodes with the anode irradiated by solar light. With a voltage of 1.3 V, the system current density is around 1  $\text{mA}/\text{cm}^2$  and it increases to 2.2  $\text{mA}/\text{cm}^2$  with a voltage of 1.65 V (1.55 V vs RHE of the anode).

The amounts of  $\text{H}_2$  and  $\text{O}_2$  produced in 2 h with electrodes  $\alpha\text{-Fe}_2\text{O}_3$  and P1 to P7 are shown in Fig. 3c. The mole ratio between  $\text{H}_2$  and  $\text{O}_2$  productions are around  $2 \pm 0.25$ , which confirms that water splitting occurs. As the film catalysts, the amounts of  $\text{H}_2$  produced are in the range of 2–14  $\mu\text{mol}/\text{cm}^2/\text{h}$  for each sample. Reported to the weight of catalyst, the amount of  $\text{H}_2$  produced even reach values as high 100  $\text{mmol}/\text{g}/\text{h}$ , which is very high for photocatalytic water splitting (Fig. S8 in the Supporting information). Such a value indicates that it is still possible to improve the photocatalytic activity for water splitting by ensuring sufficient charge separation. True water splitting occurs with no loss of  $\text{OH}^-$  showing as a constant  $\text{pH} = 12.7$  before and after the reaction for 12 h. For the reduction process, the faradaic efficiencies of the photocatalytic process were found to be around 80% for all samples (Table S1 in the Supporting information), which is not as high as electrochemical water splitting process but remarkably high for a photocatalytic process. Based on  $\text{H}_2$  production and faradaic efficiency, the best photocatalysts are P3 and P5. Furthermore, their activities are stable with a reduction of 2% after 5 h reaction for both samples (Fig. S9 in the Supporting information).

With this  $\text{Fe}_2\text{O}_3$ -based anode, the full processes of OER and HER can be defined as an electrical enhanced photocatalytic process for overall water splitting at a low applied voltage ( $< 1.60$  V vs RHE). Indeed, although at 1.60 V, OER measured in darkness is neglectable, under illumination, the maximum number of photogenerated charges are extracted from the system and converted into  $\text{O}_2$  and  $\text{H}_2$ , respectively. Therefore, in this system, the main energy conversion is the solar energy into chemical energy based on the  $\text{Fe}_2\text{O}_3$  photocatalyst, while the electrical bias application is used to improve the separation of photo-generated charges. The mechanism of the PEC water splitting is illustrated in Fig. 3d. In a traditional photocatalytic water splitting process,

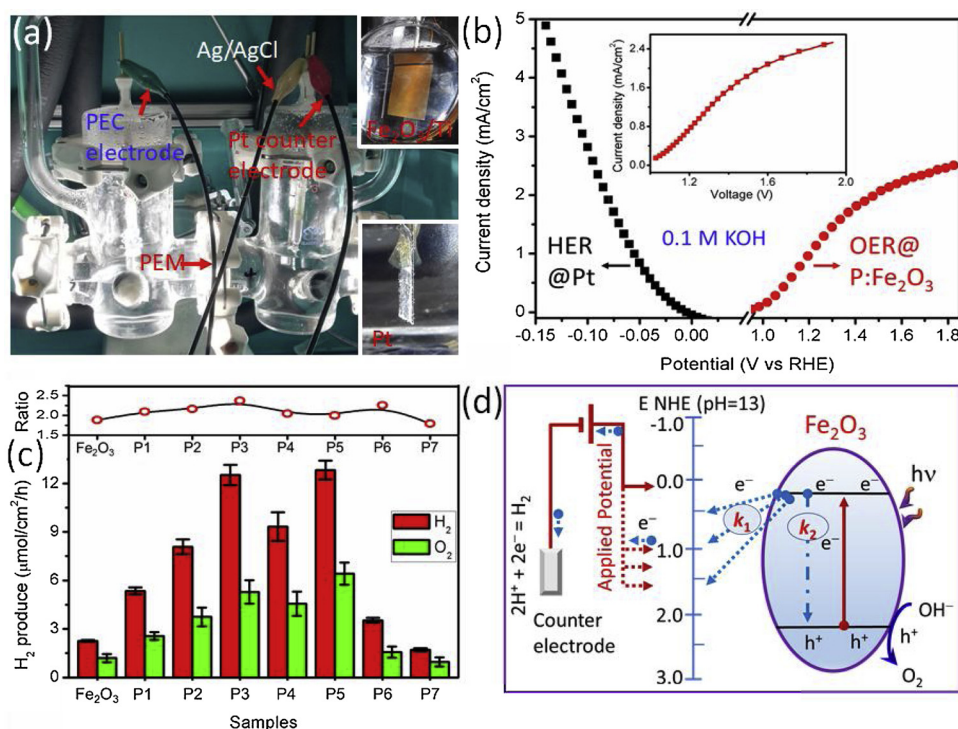
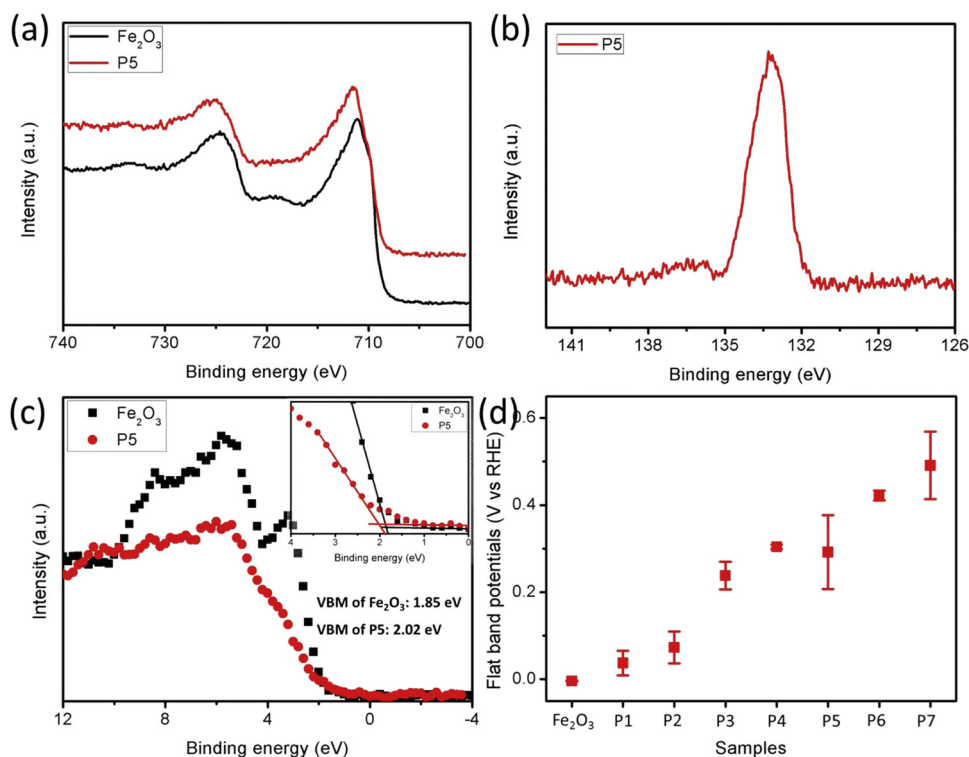


Fig. 3. (a) Photograph of the PEC cell during the photocatalytic water splitting. Insets are the photographs of the PEC electrode/Pt electrode under light irradiation. (b) LSV curves on the OER electrode and HER electrodes. Inset shows the current vs. the voltage applied on the electrodes. (c) Rate of  $\text{H}_2$  and  $\text{O}_2$  production during PEC water splitting, as well as ratio between  $\text{H}_2$  and  $\text{O}_2$ . (d) Schematic illustration of the enhanced photocatalytic water splitting under electrical bias.



**Fig. 4.** XPS spectra of (a) Fe 2p in  $\alpha$ -Fe<sub>2</sub>O<sub>3</sub> and P5 samples, (b) P 2p in P5 sample. (c) Valence band maximum (VBM) of  $\alpha$ -Fe<sub>2</sub>O<sub>3</sub> and P5 samples. Inset is the zoom-in of the VBM result. (d) Flat band potentials of the samples  $\alpha$ -Fe<sub>2</sub>O<sub>3</sub>, P1 to P7 analyzed from the Mott-Schottky plots.

the photo-induced electron will react with  $H^+$  or recombine with the holes. When a bias voltage is applied, this electric field provides a route for the electron transport. The competition between the charge transfer ( $k_1$ ) and charge recombination ( $k_2$ ) determines the efficiency of photo-generated charges. As discussed in Fig. 2, with the increase of the applied bias, the detected photo-current increases. Without more photo-induced charges generation at a constant light illumination intensity, the increased photo-current should be assigned to the domination of the charge transfer ( $k_1$ ) along with the suppression of charge recombination ( $k_2$ ). Therefore, the bias application works well for electron-hole separation, resulting in a photocatalytic activity for water splitting with a high faradaic efficiency.

To discuss the effect of phosphorous treatment on  $\alpha$ -Fe<sub>2</sub>O<sub>3</sub>, the XPS spectra, valence band maximum (VBM) measurement, and the variation of the flat band potentials obtained by Mott-Schottky plots are shown in Fig. 4. The survey of the  $\alpha$ -Fe<sub>2</sub>O<sub>3</sub> and P5 sample show the similar peaks, and the phosphorus is detected in P5 sample (Fig. S10 in the Supporting information). As shown in Fig. 4a, the XPS spectra of Fe 2p are similar in Fe<sub>2</sub>O<sub>3</sub> and P5 samples which is expected due to the low amount of P compared to Fe. The peak of P 2p lies at 133.2 eV (Fig. 4b) while that of the elemental phosphorus lies at 130.1 eV, which is coherent with the reaction of phosphorus and Fe<sub>2</sub>O<sub>3</sub> [41,42]. Moreover, this binding energy of 133.2 eV is higher than the reported value for phosphates, but it is quite consistent with the one for FePO<sub>4</sub> (133.4 eV) [36,37]. Since no Fe-P bonds are observed by XPS, the phosphorous reacts with lattice oxygen, thus locally reducing Fe<sub>2</sub>O<sub>3</sub>. This kind of doping enhances the n-character of the semiconductor. The weak XPS signal of the Ti substrate is due to the thick Fe<sub>2</sub>O<sub>3</sub> layers (Fig. S11 in the Supporting information).

The photo-response property of a photocatalyst depends on the band structure of the semiconductor which was characterized here by the VBM measurement (Fig. 4c), the flat band potentials (Figs. 4d and S12 in the Supporting information), and the UV-VIS absorption spectra (Fig. S13 in the Supporting information). The VBM of  $\alpha$ -Fe<sub>2</sub>O<sub>3</sub> is found at 1.85 eV, while that of P5 sample is around 2.02 eV. The UV-VIS

absorption spectra indicate that the 2.07 eV band gap of  $\alpha$ -Fe<sub>2</sub>O<sub>3</sub> remains the same with samples which contains phosphorous. Phosphorous doping results in a shift of the band to higher energy, resulting in a higher oxidation potential of the holes, which benefits the OER process. The flat band potentials were also obtained from the Mott-Schottky plots (Fig. S14 in the Supporting information). They become more positive with the increase of phosphorus doping concentration (Fig. 4d) in agreement with the VBM measurement, and the band gap diagrams of  $\alpha$ -Fe<sub>2</sub>O<sub>3</sub>.

For the water splitting reaction, the mass transfer of the reactants and products are also important. Using the catalytic electrode as a film would lead to mass transfer limitations because a space charge (depletion) layer is formed at the semiconductor/liquid junction [43]. Upon irradiation, photo-generated carriers are separated by the space-charge field, and the minority carriers (holes for an n-type photoanode) travel to the semiconductor/liquid junction to perform half of the water splitting reaction. With the phosphorous doping, the catalytic films show a lower mass transfer resistance (Fig. S15 and S16 in the Supporting information). Therefore, the charge transfer is improved which leads to a higher OER performance. The modification of the depletion layer upon phosphorus doping could be attributed to the surface modification during the phosphorus treatment. Interestingly, all samples exhibit a highly hydrophilic surface (Fig. S17 in the Supporting information), therefore surface wetting should not be a limitation in the modification of the depletion layer for phosphorus doped hematite. When the electrode was prepared on a Ti mesh in order to improve the mass transport in the electrolyte, no obvious improvement was found (Figs. S18 and S19 in the Supporting information). It indicates that the mass transfer limitation is not highly relying on the configuration of the Fe<sub>2</sub>O<sub>3</sub> electrode.

#### 4. Conclusion

In this work, phosphorous doped hematite nanorod films supported on titanium foils were studied. The effect of the phosphorous doping

was shown to modify the band structure, leading to a high electron density and a more positive VB band which benefits the photo-induced charge density and the hole transfer, respectively. Thus, it results in an enhancement of the OER property. The photo-induced electrons were responsible for the efficient HER at the Pt counter electrode. The high H<sub>2</sub> production rate for an electro-photocatalytic process, coupled to the high faradaic efficiencies with an applied bias indicates that such structures are of high application potential for the generation of renewable energy.

## Acknowledgements

The authors would thank Prof. Robert I. Boughton from Bowling Green State University (USA) for the help of English writing. This work was supported by the National Key Research and Development Program of China (2017YFE0102700), National Natural Science Foundation of China (Grant Nos. 51732007), and the Fundamental Research Funds of Shandong University (2018WLJH64).

## Appendix A. Supplementary data

Supplementary data associated with this article can be found, in the online version, at <https://doi.org/10.1016/j.apcatb.2019.02.048>.

## References

- [1] T.M. Su, Q. Shao, Z.Z. Qin, Z.H. Guo, Z.L. Wu, *ACS Catal.* 8 (2018) 2253–2276.
- [2] F.E. Osterloh, *Chem. Soc. Rev.* 42 (2013) 2294–2320.
- [3] L.D. Li, J.Q. Yan, T. Wang, Z.J. Zhao, J. Zhang, J.L. Gong, N.J. Guan, *Nat. Commun.* 6 (2015) 5881.
- [4] X.B. Chen, L. Liu, F.Q. Huang, *Chem. Soc. Rev.* 44 (2015) 1861–1885.
- [5] A. Sinhamahapatra, J.P. Jeon, J.S. Yu, *Energy Environ. Sci.* 8 (2015) 3539–3544.
- [6] M.J. Xu, Y. Chen, J.T. Qin, Y.W. Feng, W. Li, W. Chen, J. Zhu, H.X. Li, Z.F. Bian, *Environ. Sci. Technol.* 52 (2018) 13879–13886.
- [7] J.W. Ng, S.P. Xu, X.W. Zhang, H.Y. Yang, D.D. Sun, *Adv. Funct. Mater.* 20 (2010) 4287–4294.
- [8] J.Q. Wen, J. Xie, H.D. Zhang, A.P. Zhang, Y.J. Liu, X.B. Chen, X. Li, *ACS Appl. Mater. Interfaces* 9 (2017) 14031–14042.
- [9] Y.X. Zhang, M.J. Xu, H. Li, H. Ge, Z.F. Bian, *Appl. Catal. B: Environ.* 226 (2018) 213–219.
- [10] K. Chang, Z.W. Mei, T. Wang, Q. Kang, S.X. Ouyang, J.H. Ye, *ACS Nano* 8 (2014) 7078–7087.
- [11] Y.H. Sang, Z.H. Zhao, J. Tian, P. Hao, H.D. Jiang, H. Liu, J.P. Claverie, *Small* 10 (2014) 3775–3782.
- [12] M. Tabata, K. Maeda, T. Ishihara, T. Minegishi, T. Takata, K. Domen, *J. Phys. Chem. C* 114 (2010) 11215–11220.
- [13] X. Zong, H.J. Yan, G.P. Wu, G.J. Ma, F.Y. Wen, L. Wang, C. Li, *J. Am. Chem. Soc.* 130 (2008) 7176–7177.
- [14] Z.F. Huang, J.J. Song, X. Wang, L. Pan, K. Li, X.W. Zhang, L. Wang, J.J. Zou, *Nano Energy* 40 (2017) 308–316.
- [15] K. Maeda, T. Takata, M. Hara, N. Saito, Y. Inoue, H. Kobayashi, K. Domen, *J. Am. Chem. Soc.* 127 (2005) 8286–8287.
- [16] S.S. Chen, Y. Qi, T. Hisatomi, Q. Ding, T. Asai, Z. Li, S.S.K. Ma, F.X. Zhang, K. Domen, C. Li, *Angew. Chem. Int. Ed.* 54 (2015) 8498–8501.
- [17] Y.G. Tan, Z. Shu, J. Zhou, T.T. Li, W.B. Wang, Z.L. Zhao, *Appl. Catal. B: Environ.* 230 (2018) 260–268.
- [18] H.J. Yan, Y. Xie, Y.Q. Jiao, A.P. Wu, C.G. Tian, X.M. Zhang, L. Wang, H.G. Fu, *Adv. Mater.* 30 (2018) 1704156.
- [19] X.F. Zhang, Y.N. Wang, B.S. Liu, Y.H. Sang, H. Liu, *Appl. Catal. B: Environ.* 202 (2017) 620–641.
- [20] H.D. Li, Y.H. Sang, S.J. Chang, X. Huang, Y. Zhang, R.S. Yang, H.D. Jiang, H. Liu, Z.L. Wang, *Nano Lett.* 15 (2015) 2372–2379.
- [21] Y.W. Feng, H. Li, L.L. Ling, S. Yan, D.L. Pan, H. Ge, H.X. Li, Z.F. Bian, *Environ. Sci. Technol.* 52 (2018) 7842–7848.
- [22] X.N. Wang, F.L. Wang, Y.H. Sang, H. Liu, *Adv. Energy Mater.* 7 (2017) 1700473.
- [23] X.Y. Yu, X.W. (David) Lou, *Adv. Energy Mater.* 8 (2018) 1701592.
- [24] J.X. Zhu, Z.Y. Yin, D. Yang, T. Sun, H. Yu, H.E. Hoster, H.H. Hng, H. Zhang, Q.Y. Yan, *Energy Environ. Sci.* 6 (2013) 987–993.
- [25] L. Wang, H.W. Wei, Y.J. Fan, X. Gu, J.H. Zhan, *J. Phys. Chem. C* 113 (2009) 14119–14125.
- [26] W. Wu, S.F. Zhang, X.H. Xiao, J. Zhou, F. Ren, L.L. Sun, C.Z. Jiang, *ACS Appl. Mater. Interfaces* 4 (2012) 3602–3609.
- [27] Z. Lou, F. Li, J.N. Deng, L.L. Wang, T. Zhang, *ACS Appl. Mater. Interfaces* 5 (2013) 12310–12316.
- [28] A. Kay, I. Cesar, M. Grätzel, *J. Am. Chem. Soc.* 128 (2006) 15714–15721.
- [29] Q. Yu, X.G. Meng, T. Wang, P. Li, J.H. Ye, *Adv. Funct. Mater.* 25 (2015) 2686–2692.
- [30] M. Barroso, C.A. Mesa, S.R. Pendlebury, A.J. Cowan, T. Hisatomi, K. Sivula, M. Grätzel, D.R. Klug, J.R. Durrant, *PNAS* 109 (2012) 15640–15645.
- [31] I. Cesar, A. Kay, J.A.G. Martinez, M. Grätzel, *J. Am. Chem. Soc.* 128 (2006) 4582–4583.
- [32] J.S. Jang, J. Lee, H. Ye, F.-R.F. Fan, A.J. Bard, *J. Phys. Chem. C* 113 (2009) 6719–6724.
- [33] A. Bak, W. Choi, H. Park, *Appl. Catal. B: Environ.* 110 (2011) 207–215.
- [34] Z.W. Fu, T.F. Jiang, Z.P. Liu, D.J. Wang, L.L. Wang, T.F. Xie, *Electrochim. Acta* 129 (2014) 358–363.
- [35] Y.S. Hu, A. Kleiman-Shwarsstein, A.J. Forman, D. Hazen, J.-N. Park, E.M. McFarland, *Chem. Mater.* 20 (2008) 3803–3805.
- [36] Y.C. Zhang, S.Q. Jiang, W.J. Song, P. Zhou, H.W. Ji, W.H. Ma, W.C. Hao, C.C. Chen, J.C. Zhao, *Energy Environ. Sci.* 8 (2015) 1231–1236.
- [37] Z.B. Luo, C.C. Li, S.S. Liu, T. Wang, J.L. Gong, *Chem. Sci.* 8 (2017) 91–100.
- [38] Y.L. Wang, J.J. Xu, H. Wu, M. Xu, Z. Peng, G.F. Zheng, *J. Mater. Chem.* 22 (2012) 21923–21927.
- [39] G. Horowitz, *J. Electroanal. Chem.* 159 (1983) 421–436.
- [40] J.M. Bolts, M.S. Wrighton, *J. Phys. Chem.* 80 (1976) 2641–2645.
- [41] X.D. Yan, Y.H. Yu, X.P. Yang, *RSC Adv.* 4 (2014) 24986–24990.
- [42] F. Niu, L.M. Tao, Y.C. Deng, Q.H. Wang, W.G. Song, *New J. Chem.* 38 (2014) 2269–2272.
- [43] D.J. Blackwood, *Electrochim. Acta* 46 (2000) 563–569.